Korean J. Chem. Eng., 32(11), 2227-2235 (2015)
DOI: 10.1007/s11814-015-0059-1

pISSN: 0256-1115
eISSN: 1975-7220

Desulfurization of coke oven gas using char-supported Fe-Zn-Mo catalysts: Mechanisms and thermodynamics

Jinxiao Dou*, Xianchun Li*, Arash Tahmasebi*, Jing Xu*, and Jianglong Yu*,,†**

*Key Laboratory for Advanced Coal and Coking Technology of Liaoning Province, School of Chemical Engineering, University of Science and Technology Liaoning, Anshan 114051, China
**Chemical Engineering, University of Newcastle, Callaghan, NSW 2308, Australia
(*Received 24 December 2014 • accepted 30 March 2015*)

Abstract−Sulfidation properties of char-supported Fe-Zn-Mo sorbents prepared by ultrasonic impregnation method were investigated during simultaneous removal of H_2S and COS from coke oven gas (COG) using a fixed-bed quartz reactor. Sorbent samples before and after sulfidation were analyzed using X-Ray diffraction (XRD) and Fourier transform infrared spectroscopy (FT-IR). The experimental results showed that the addition of Mo significantly improved the desulfurization properties (i.e., breakthrough time, sulfur capacity and desulfurization efficiency) of Fe-Zn sorbents. Desulfurization reactions were exothermic and thermodynamically favorable in the temperature range of 200-400 °C. Thermodynamic analysis of the sorbents indicated that higher concentration of H_2S and lower concentration of H_2 favors the reaction of metal oxides with H_2S to form metal sulfides.

Keywords: Coke Oven Gas, Sulfidation, Char-supported Sorbents, Sulfur Capacity

INTRODUCTION

Coke oven gas from the coking industry contains H_2, CO, CO_2 and CH_4, as well as sulfur containing species (H_2S, COS) and nitrogen compounds (NH_3, HCN) [1-3]. These impurities must be removed to reduce the emissions of air pollutants and prevent the corrosion of downstream equipment and catalyst deactivation. The conventional desulfurization processes such as wet desulfurization operate at low temperatures and need large investment and high operational cost. In comparison, dry desulfurization has the potential to significantly improve thermal efficiency and reduce capital costs [4,5]. However, dry desulfurization processes require sorbents which may achieve sulfur cleaning down to sub-ppm levels with fast adsorption kinetics, mechanical, chemical and thermal stability, etc. It is reported that metal oxide sorbents have the potential to achieve these goals [6]. Previous desulfurization efforts using single, binary, and ternary sorbents based on iron, calcium, manganese, zinc, copper and molybdenum etc. have been reported in the literature [7,8]. In more recent studies by the authors, activated char-supported Fe-based sorbents showed the potential to remove sulfur and nitrogen containing impurities simultaneously [9-11]. Zinc-based sorbents are very effective for removal of H_2S due to their high equilibrium constant for sulfidation and thermal stability [12-14]. Copper-based sorbents have the highest sulfidation equilibrium constants and can remove H_2S from several thousand ppm to sub-ppm level. The addition of small amounts of copper oxide into iron containing sorbents may significantly increase its reactivity. However, copper compounds have relatively low melting point, which limits their application [15,16]. Mo is reported to effectively improve the desulfurization efficiency and increase the mechanical strength of the sorbent [17,18]. Zhao et al. [19] reported that doping of Fe-Mn mixed oxides with rare-earth oxides greatly improved the sulfur absorption capacity despite their low BET surface area and porosity. Bao et al. [20] claimed that MgO improved the sulfur removal efficiency and the sulfur retention capacity of iron-based sorbents. MCM-41 supported $La_xFe_yO_z$ (La : Fe=1 : 2) sorbent also showed high performance and stability for hot coal gas desulfurization [21]. Meanwhile, the mechanism and thermodynamics of the char-supported Fe-based sorbents have not been systematically studied. This paper is focused on the sulfidation properties of char-supported Fe-Zn-Mo sorbents. The mechanism and thermodynamic properties of the sorbents during sulfidation reactions are systematically investigated.

EXPERIMENTAL SECTION

1. Sorbent Preparation

Shenhua lignite from Inner Mongolia region of China was used in this study. The samples were crushed and sieved to a particle size range of 75-125 μm and then dried in N_2 atmosphere at 105 °C. The coal sample was first acid-washed using 0.4 N HCL aqueous solution while being stirred for 12 h. The slurry was then filtered and washed with de-ionized water until its pH value became constant (5.0-5.5). Co-precipitation processes were used for Zn and Fe loading onto the acid-washed coal. The ratio of ferric nitrate to acid-washed coal was 1 : 10 by weight. $Fe(NO_3)_3{\cdot}9H_2O$, $Zn(NO_3)_2{\cdot}6H_2O$, and $(NH_4)_6Mo_7O_{24}{\cdot}4H_2O$ were used for impregnation to produce sorbents with Fe : Zn : Mo molar ratios of 2 : 1 : 0.5, 2 : 1 : 1 and 2 : 1 : 2. The acid-washed coal was mixed with ferric nitrate and zinc nitrate aqueous solutions followed by ultrasonic-assisted impregnation for

†To whom correspondence should be addressed.
E-mail: jianglong.yu@newcastle.edu.au, jianglongyu@163.com

5 h at 50 °C. Ammonia aqueous solution was then added gradually to the mixture until the solution pH reached to 10. The ultrasound irradiation was continuously applied for 1 h. The slurry was then filtered and washed by using de-ionized water. The samples were then dried at 105 °C and gasified for 30 min in steam (15% vol. balanced with nitrogen) in a fluidized-bed quartz reactor. The prepared sorbents were assigned as M5, Z6, F10, F10Z6 and F10Z6M5 and their compositions are given in Table 2.

2. Desulfurization Experiments

The desulfurization experiments were carried out in the temperature range of 200-400 °C in a vertical quartz fixed-bed reactor with an internal diameter of 2 cm. 1.2 g sorbent was charged into the reactor for each experiment. After the desired reaction temperature was reached, the simulated coal gas was passed through the fixed-bed reactor and the outlet gas composition (H_2S and COS) was measured with a GC equipped with a flame photometric detector (FPD) and a thermal conductivity detector (TCD). The limit for detection of sulfur gases was 1 ppmv and the H_2S and COS concentrations smaller than 1 ppmv were not detected by the GC. Conditions used in the experiments are shown in Table 1.

The sulfur capacity of sorbent at breakthrough point and the conversion of the sorbents (X) were calculated by Eqs. (1) and (2), respectively.

$$S = \frac{\nu_{sp} V_{bj} M_s}{m_s V_m} \times \left[\int_0^t (C_{in} - C_{out}) dt \right] \times 10^{-4} \quad (1)$$

$$X = \frac{\text{Actual sulfur capacity}}{\text{Theoretical sulfur capacity}} \times 100\% \quad (2)$$

Table 1. Experimental conditions used in this study

Temperature (°C)		200-400
Flow rate (ml/min)		17.5
Coke oven gas compositions (%)	CO	7.14
	CO_2	2.55
	H_2	60.34
	CH_4	25.79
	H_2S	0.336
	COS	0.0140
	N_2	Balance
Particle size (mm)		0.075-0.125

where, S is the effective sulfur capacity of sorbent; ν_{sp} is the space velocity (h^{-1}); V_{bj} is the volume of sorbents in the reactor (l); M_s is molar mass of sulfur (32 g/mol); m_s is the weight of sorbent in the reactor (g); V_m is molar volume of H_2S at 1atm and 25 °C (24.5 l/mol); t is the breakthrough time of sorbent (h); C_{in} and C_{out} are the inlet and outlet concentration of H_2S (COS) (ppmv), respectively.

Theoretical sulfur capacity of the sorbents is defined as the theoretical sulfur uptake of all active components in sorbents and is the mass of sulfur adsorbed on 100 g sorbent.

3. Sorbent Characterization

The surface area and pore structure of the sorbents were analyzed by Brunauer-Emmett-Teller (BET) analyzer (ASAP2020) using N_2 gas adsorption. Specific surface area and pore volume were calculated based on N_2 adsorption isotherm. The t-plot theory was employed to calculate the micropore surface area (S_{Mi}) and micropore volumes (V_{Mi}).

Inductively coupled plasma-atomic emission spectrometry (ICP-AES WLY100-1, Beijing Haiguang) was used to measure the chemical composition of the sorbents. Solid crystal structures were identified by Shimadzu 7000 powder X-ray diffraction (XRD). The Cu Kα radiation operated at 30 mA and 40 kV. The scattered intensity was collected at a rate of 3° min^{-1} over a 2θ range of 10-80°. Infrared (IR) spectra of sorbent before and after desulfurization were obtained with a Thermo Fisher Nicolet IS5 mid-FT-IR spectrometer. Samples were prepared by grinding 1.0 mg of desulfurization sorbent with 100 mg KBr.

Thermodynamic calculations involved commercially available HSC software. Gibbs energy minimization module was used to calculate the phase stability diagrams. The relevant thermodynamic constants and data were selected from the HSC Chemistry Database.

RESULTS AND DISCUSSION

1. Pore Structure of Sorbents

Fig. 1 shows the nitrogen adsorption isotherms of the sorbents with different compositions. Based on the IUPAC analysis, all sorbents displayed type I isotherms except for char and M5 sorbents, indicating that the char-supported metal oxide sorbents possessed characteristics of porous solids with small mesopores [12]. This type of isotherm could be either due to the presence of very narrow mesopores or a bimodal distribution having one maximum in the micropore and another in the mesopore range [22]. Char and M5 sorbents showed mesoporous structure with narrow pore-size

Table 2. Composition, breakthrough sulfur capacity and conversion of sorbents

Sorbent sample	Composition (wt%)			Breakthrough sulfur capacity (g S per 100 g sorbent)	Theoretical sulfur capacity (g S per 100 g sorbent)	Conversion of sorbent (%)
	Mo	Fe	Zn			
M5	6.32	/	/	0.35	0.59	59.11
Z6	/	/	6.82	2.78	5.10	54.50
F10	/	15.31	/	11.28	19.97	56.48
F10Z6	/	14.30	5.60	13.91	22.40	62.10
F10Z6M5	5.76	15.61	4.85	15.24	23.25	65.56
F10Z6M10	8.36	13.72	4.31	14.13	24.25	58.27
F10Z6M20	11.21	13.31	3.62	9.16	18.20	50.34

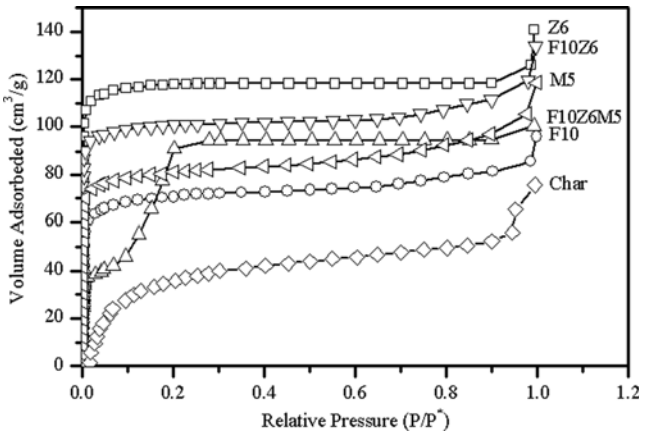

Fig. 1. Nitrogen adsorption isotherms of different sorbents from BET analysis.

Table 3. Structural parameters of different sorbents

Samples	S_{BET} (m^2/g)	S_{Mi} (m^2/g)	V_t (cm^3/g)	V_{Mic} (cm^3/g)	D_a (nm)
Char	62.59	58.38	0.18	0.03	0.80
M5	109.65	90.84	0.27	0.04	1.35
Z6	430.07	334.07	0.21	0.17	1.27
F10	268.88	206.39	0.15	0.10	1.27
F10Z6	390.19	298.71	0.21	0.15	1.09
F10Z6M5	370.65	260.49	0.20	0.13	1.15

*S_{BET}: total surface area; S_{Mi}: microporous surface area; V_t: total pore volume; V_{Mic}: micropore volume; D_a: average pore diameters

distributions. The physical properties (BET surface area, pore volume and average pore size) of different sorbent samples are given in Table 3. The average pore diameter and surface area of sorbents increased significantly with impregnation of multiple active components. Sorbents also showed a mesoporous structure as evidenced by the values of microporous surface area (S_{Mi}). Micropore surface area and micropore volume of char-supported metal sorbents were dominant. This suggests that the loading of metals (Zn, Fe, Mo) into char leads to the promotion of micropore structure.

2. Sulfidation of F10Z6 Sorbent

The desulfurization curves of the F10Z6 sorbent at different temperatures are shown in Fig. 2. The F10Z6 sorbent reduced the concentration of both H_2S and COS to negligible level at all reaction temperatures prior to breakthrough point. The breakthrough time increased significantly with increasing sulfidation temperature from 200 °C to 400 °C during both H_2S and COS removal. The H_2S breakthrough curve shows that the breakthrough time increased from 117 min at 200 °C to 663 min 300 °C. At 400 °C, the F10Z6 sorbent had a breakthrough time of 1,402 min and exhibited the highest sulfur capacity of 17.70 (g S per 100 g sorbent). This value was close to theoretical sulfur capacity of 18.10 (g S per 100 g sorbent). The breakthrough time during the removal of COS (Fig. 2(b)) was similar to that for H_2S. This indicates that char-supported F10Z6 sorbent can simultaneously remove H_2S and COS under all sulfidation conditions tested in this study. After breakthrough at 400 °C, the outlet concentration of COS decreased while that of H_2S increased to even higher level than the inlet H_2S concentration. This can be explained by the catalytic hydrolysis reaction of COS by ZnS and $ZnFe_2O_4$ and sulfidation temperatures. This observation is consistent with the literature [23].

3. FT-IR Analysis of F10Z6 Sorbent

The FT-IR spectra of char-supported F10Z6 sorbent before and after desulfurization at different temperatures in 1,600-400 cm^{-1} zone are shown in Fig. 3. The adsorption bands at 865, 798 and 1,087 cm^{-1} corresponded to bending, symmetric, and asymmetric vibration modes of silicon oxide, respectively [24]. The band at around 1,600 cm^{-1} was assigned to aromatic carbon, and aromatic ring stretch groups [25]. The band at 433 cm^{-1} was assigned to the vibrations of Zn-O bonds [26]. The absorption band at 585 cm^{-1} corresponded to vibrations of Fe-O-Fe [27]. After desulfurization at 300 °C and 400 °C, the intensity of Zn-O and Fe-O bands decreased due to their reaction with sulfur species. These observations confirmed that Zn-O and Fe-O reacted with H_2S to form Zn-S [28] and Fe-S [29].

4. Sulfidation of F10Z6M5 Sorbent

The sulfidation behavior of F10Z6M5 sorbent at different tem-

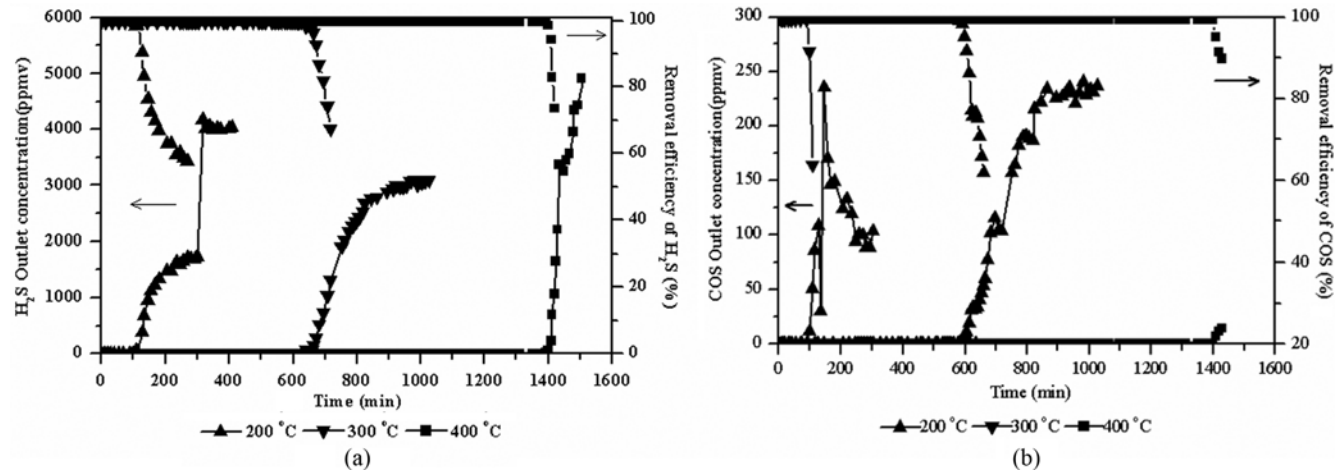

Fig. 2. Sulfidation curves at different temperatures for the F10Z6 sorbent: (a) H_2S; (b) COS.

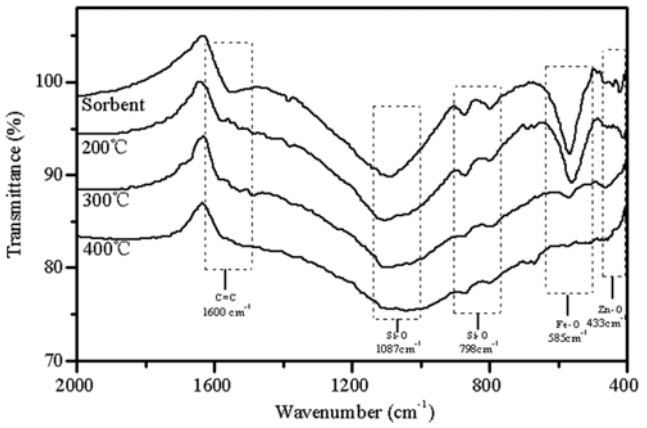

Fig. 3. FT-IR spectra of the FZ2 sorbent after sulfidation at different temperatures.

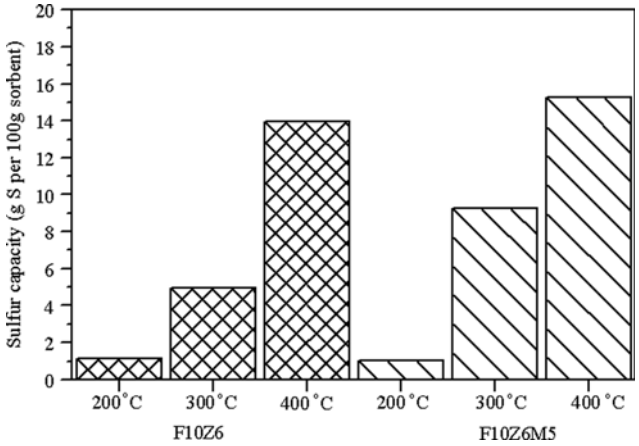

Fig. 5. Sulfur capacity of different sorbents at different sulfidation temperatures.

peratures is shown in Fig. 4. The breakthrough time and desulfurization efficiency of H_2S increased with increasing sulfidation temperature from 200 to 400 °C. The breakthrough times of F10Z6M5 sorbent were 93, 925 and 1,765 min at 200, 300, and 400 °C, respectively, which indicated that the sulfidation temperature had a significant effect on desulfurization performance of the sorbents. Sulfur capacity of the sorbent was also increased at higher temperatures. Comparison of the breakthrough sulfur capacities of char-supported F10Z6 and F10Z6M5 sorbents is shown in Fig. 5. Sulfur capacities of these sorbents were very low at 200 °C, indicating that metal oxides have a low reactivity at low temperatures. When the desulfurization temperature was increased to 300 °C and 400 °C, the F10Z6M5 sorbent had a higher sulfur capacity than that of the F10Z6 sorbent. The sulfur capacity of F10Z6M5 sorbent was 1.02, 9.28, and 15.24 (g S per 100 g sorbent) at 200, 300 and 400 °C, respectively. It can be concluded that 400 °C is the optimal desulfurization temperature under conditions used in this study. These results indicated that sulfidation temperature is a key factor affecting the performance of desulfurization sorbents.

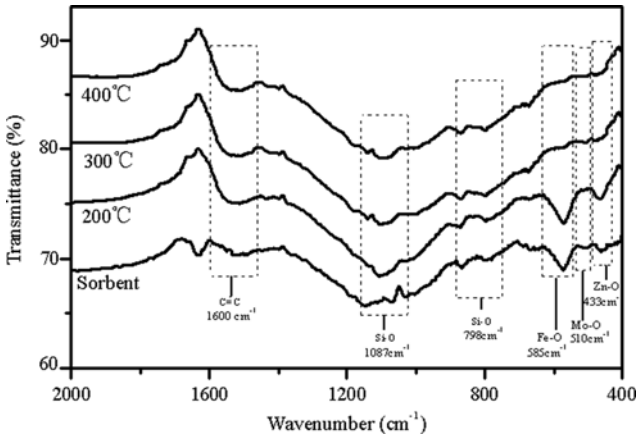

Fig. 6. FT-IR analysis of F10Z6M5 sorbent after sulfidation at different temperatures.

5. FT-IR Analysis of F10Z6M5 Sorbent

Fig. 6 shows the IR spectra of F10Z6M5 sorbent before and after sulfidation. Significant changes occurred in the 600-400 cm^{-1} region. The band at 510 cm^{-1} was assigned to Mo-O bending vibration of MoO_2. However, as these bands disappear after sulfidation, stretch-

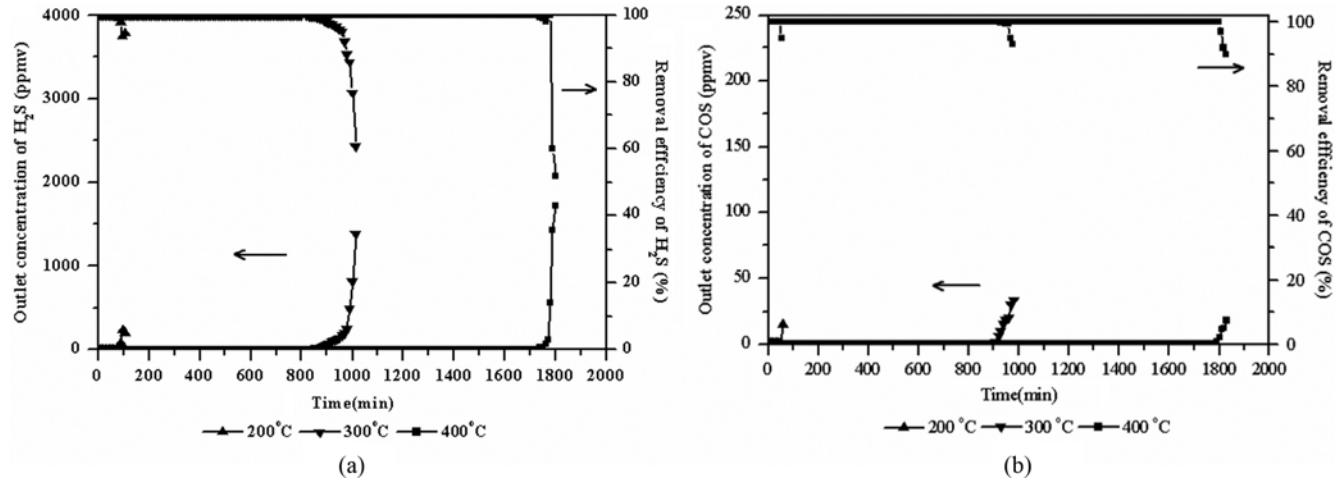

Fig. 4. Effects of sulfidation temperature on the sulfidation curves of the F10Z6M5 sorbent: (a) H_2S; (b) COS.

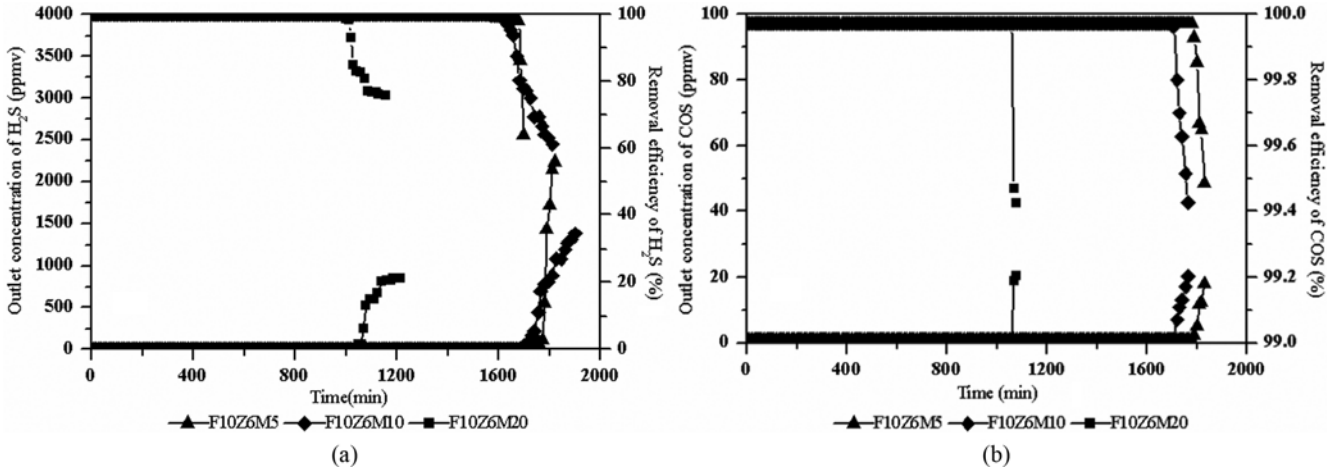

Fig. 7. The exit concentration of H_2S and COS and desulfurization efficiency of char-supported Fe-Zn-Mo sorbents with different Fe : Zn : Mo molar ratios.

ing vibration peaks of Fe-O, Zn-O, Mo-O were transformed into sulfide structures. The 610, 450, and 407 cm^{-1} regions corresponded to stretching vibration of Fe-S, Mo-S and Zn-S, respectively [30].

6. Effect of Mo in Sorbents on Desulfurization Performance

The effect of Fe : Zn : Mo molar ratio in sorbents on their desulfurization performance was investigated at 400 °C. Fig. 7 shows the exit concentration of H_2S and COS and desulfurization efficiency of char-supported Fe-Zn-Mo sorbents at different Fe : Zn : Mo molar ratios. The sulfur-containing gases (H_2S and COS) at the outlet were effectively reduced to negligible level and the desulfurization efficiency reached to nearly 100% prior to the breakthrough point. Fig. 7(a) shows that 100% desulfurization efficiency of the sorbent F10Z6M5 (molar ratio of Fe to Zn to Mo is 2 : 1 : 0.5) can be achieved for 1,765 min. However, when the F10Z6M10 sorbent with a molar ratio of Fe : Zn : Mo of 2 : 1 : 1 and F10Z6M20 sorbent with molar ratio of Fe : Zn : Mo of 2 : 1 : 2 were used, the breakthrough time decreased to 1,710 and 1,065 min. These results reveal that the addition of Mo to Fe-Zn sorbent can improve the desulfurization reactivity; however, excessively high Mo content did not promote H_2S and COS removal. Fig. 7(b) shows that COS concentration followed a similar trend for H_2S. The breakthrough sulfur capacity and conversion of all sorbents with different molar ratio of Fe : Zn : Mo are compared in Table 2. The breakthrough sulfur capacities of F10Z6M5, F10Z6M10, and F10Z6M20 sorbents were 15.24, 14.13 and 9.16 (g S per 100 g sorbent), respectively. With increasing Mo content, the conversion of Fe-Zn-Mo sorbent was noticeably decreased.

7. Sulfidation of Single Metal Oxide and Complex Metal Oxide Sorbents

Fig. 8 compares the breakthrough time and desulfurization efficiency of char-supported metal oxide sorbents at 400 °C. Breakthrough time of char-supported sorbents increased with increasing loading level of metal oxides (Zn and Mo). In Fig. 8(a), the H_2S breakthrough time of M5, Z6, F10 and F10Z6 sorbents was 43, 323, 1,305, and 1,620 min, respectively, while that of F10Z6M5 was 1,765 min, the longest among all. The COS breakthrough time followed a similar trend to that of H_2S. Fe10Z6M5 sorbent exhibited the highest desulfurization efficiency with longest breakthrough time compared to sorbents with by single metal oxide (M5, Z6 and F10) which

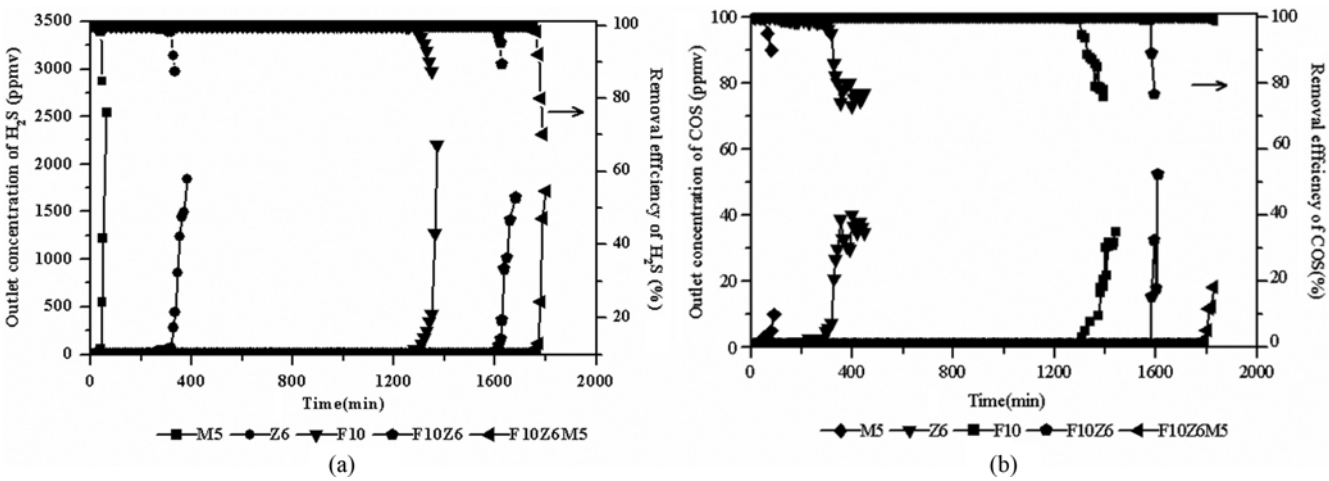

Fig. 8. Sulfidation curves of different sorbents at 400 °C: (a) H_2S; (b) COS.

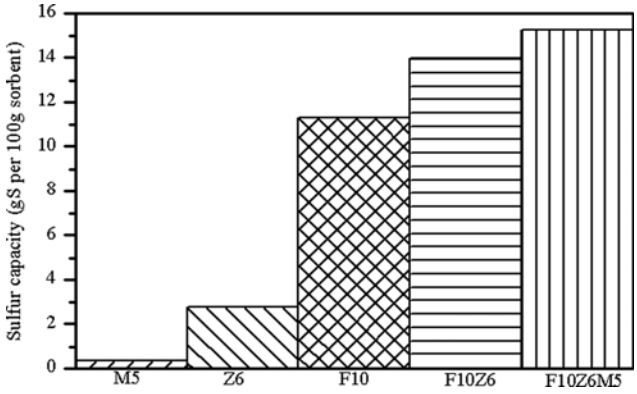

Fig. 9. Sulfur capacity of different sorbents at 400 °C.

was attributed to the addition of Mo.

Sulfur capacities of sorbents with different compositions are given in (Fig. 9). Sulfur capacity increased with increasing the content of metal oxides. The sulfur uptake of F10Z6M5 sorbent was the highest among all sorbents tested. The breakthrough sulfur capacity of M5, Z6, F10, F10Z6 and F10Z6M5 sorbents was 0.35, 2.78, 11.28, 13.91 and 15.24 (g S per 100 g sorbent), respectively (Table 2). The F10Z6M5 sorbent showed a significantly better desulfurization performance compared to single metal oxide sorbents. Also, the breakthrough sulfur capacity of F10Z6M5 sorbent was larger than the sum of F10Z6 and M5 sorbents. The addition of Mo changed the chemical structure of the char-supported iron-zinc sorbent and formed metal compounds which play an important role in H_2S and COS removal, leading to a high desulfurization reactivity. Although the total pore volume and average pore diameter of char and char-supported sorbents did not change significantly (as shown in Table 3), micropore surface area and micropore volume of sorbents was increased substantially. It should be noted that the molecular diameter of H_2S is 0.328 nm and the average pore size of sorbent is around

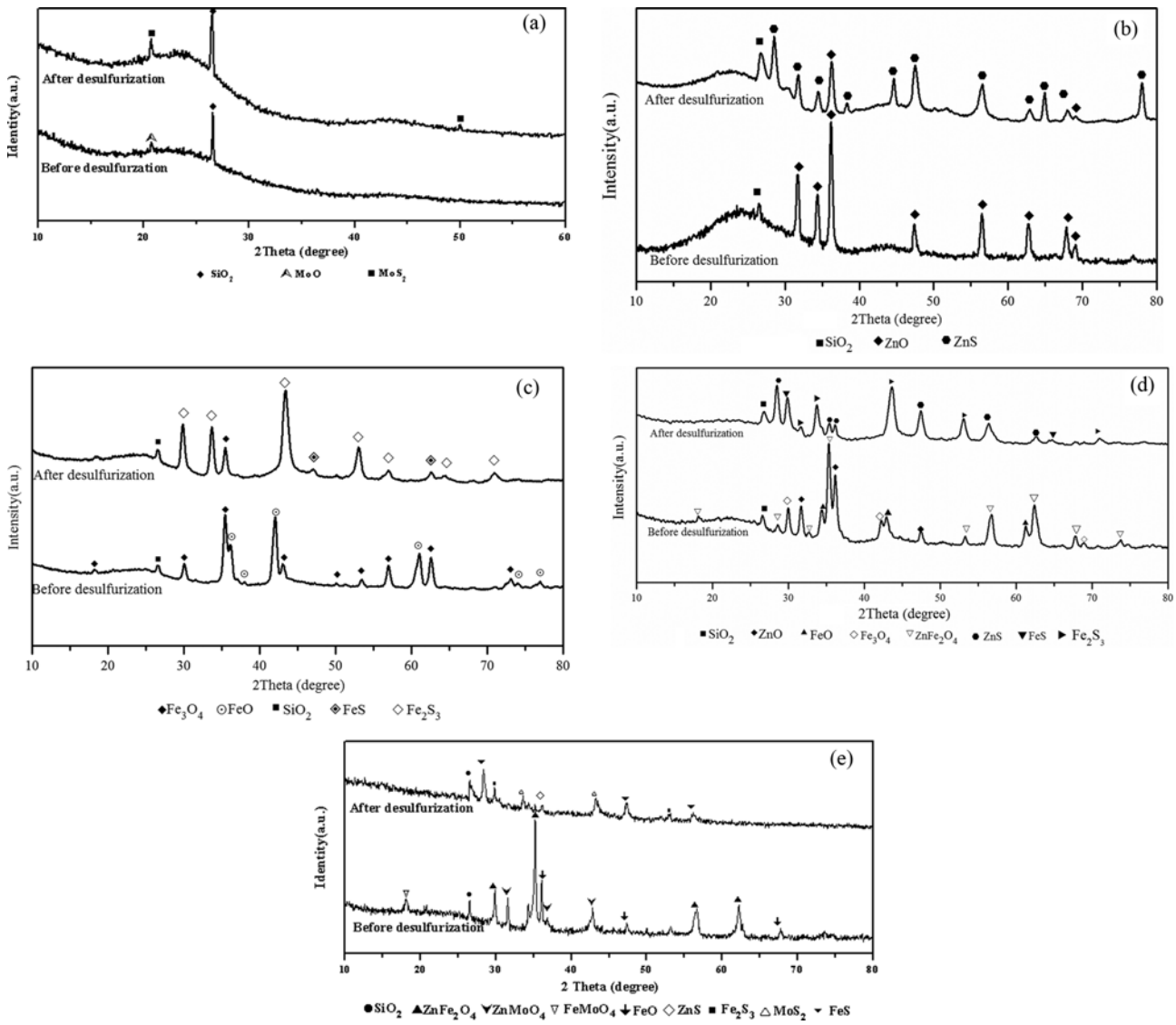

Fig. 10. XRD spectra of different sorbents before and after desulfurization: (a) M5 sorbent; (b) Z6 sorbent; (c) F10 sorbent; (d) F10Z6 sorbent; (e) F10Z6M5 sorbent.

1.2 nm. Therefore, H_2S molecules can penetrate through the micropore structure of sorbents and react with active components (metal oxides) [12]. These results further indicate that physical properties and the type of active compounds in sorbents have a significant effect on their desulfurization reactivity. The conversions of sorbents used in this study are compared in Table 2. The conversion of sorbents was calculated by comparing the breakthrough sulfur capacity and theoretical sulfur capacity. The conversion of single metal oxide sorbents (M5, Z6 and F10) was 59.11%, 54.50% and 56.48%, respectively. When zinc was added into the iron-based sorbents, the conversion (F10Z6 sorbent) reached to 62.10%. The conversion of F10Z6M5 sorbent reached to 65.56%, the highest among all sorbents used in this study.

8. XRD Analysis of the Sorbents

Fig. 10 shows XRD spectra of char-supported sorbents with different compositions before and after desulfurization. Our previous study showed that the sulfur capacity of iron-based sorbents mainly depends on the actual content of iron loaded into the char [7]. Fig. 10(a) shows that M5 sorbent contained MoO and SiO_2. After desulfurization, MoO was converted into MoS_2. ZnO was the main active component in the Z6 sorbent and was converted to ZnS after desulfurization (Fig. 10(b)). In case of F10 sorbent, Fe exists as Fe_3O_4 and FeO prior to desulfurization. After desulfurization, iron oxides were converted to FeS and Fe_2S_3 (Fig. 10(c)). In F10Z6 sorbent, the active components were in the form of Fe_3O_4, ZnO and $ZnFe_2O_4$. After desulfurization, metal oxides were converted into ZnS, Fe_2S_3 and FeS (Fig. 10(d)). $ZnFe_2O_4$, $FeMoO_4$ and $ZnMoO_4$ phase were present in F10Z6M5 sorbent before desulfurization (Fig. 10(e)). CO and H_2 have been reported to exhibit a high reactivity toward surface Zn^{2+} ions in Zn-containing catalysts at high temperature, reducing Zn^{2+} to Zn [14]. The presence of MoO on the surface of sorbent in the forms of Mo-I and Mo-II and the formation of Mo-Fe compounds improved the reactivity of iron-based sorbents. A water-gas shift reaction (WGSR) may be involved in order to elucidate this phenomenon ($CO+H_2O \rightarrow CO_2+H_2$). WGSR consumes the water that is formed during sulfidation reaction ($MO+ H_2S \rightarrow MS+H_2O$) and might occupy the active site of the active components; therefore, the desulfurization properties of sorbent may be enhanced. The desulfurization reactions can be summarized as follows: [18,31]

$$ZnO+H_2S(g) \rightarrow ZnS+H_2O; \quad K=3.2\times10^{3} \quad (3)$$

$$2ZnFe_2O_4+H_2(g)+7H_2S(g) \rightarrow 2ZnS+Fe_2S_3+8H_2O+2FeS; \quad K=2.45\times10^{8} \quad (4)$$

$$Fe_3O_4+4H_2S(g) \rightarrow FeS+Fe_2S_3+4H_2O; \quad K=1.49\times10^{2} \quad (5)$$

$$MoO_3+2H_2S(g)+H_2(g) \rightarrow MoS_2+3H_2O; \quad K=3.7\times10^{10} \quad (6)$$

$$2FeMoO_4+7H_2S(g)+H_2(g) \rightarrow 8H_2O+Fe_2S_3+2MoS_2; \quad K=4.6\times10^{16} \quad (7)$$

$$ZnMoO_4+4H_2S(g) \rightarrow ZnS+MoS_2+4H_2O+S; \quad K=1.7\times10^{8} \quad (8)$$

9. Thermodynamic Analysis of Desulfurization Reaction

The changes in Gibbs free energy (Δ_rG_m) and enthalpy (Δ_rH_m) of the above reactions in the temperature range of 0-1,000 °C were calculated (Fig. 11). These reactions are thermodynamically favorable at 400 °C at which the value of Gibbs free energy (Δ_rG_m) is negative. With increasing temperature, the value of Gibbs free energy (Δ_rG_m) increased to positive values, indicating that the reactions were not thermodynamically favorable at high temperatures. At any given temperature below 600 °C, the Gibbs free energy (Δ_rG_m) of F10Z6M5 sorbent showed the lowest value, indicating that reaction (7) was the most favorable reaction. The values of Δ_rH_m were negative (Fig. 11(b)), implying that the reactions were exothermic. The value of Δ_rH_m for reaction (7) was lowest among all the sorbents tested. These results are consistent with those reported in the literature [32]. The values of Δ_rG_m and Δ_rH_m for reaction (7) were –214.70 KJ/mol and –695.95 KJ/mol at 400 °C, respectively. As shown in Fig. 5, sulfidation temperature had a significant effect on desulfurization performance of the sorbents. Sulfur capacity of the sorbent was also increased with increasing sulfidation temperatures. Although the effect of addition of Mo in the Fe-Zn sorbents was more obvious at 300 °C, the highest sulfur capacity and desulfurization efficiency was achieved at 400 °C. Therefore, the combination of these two effects, i.e., temperature and Mo addition, was

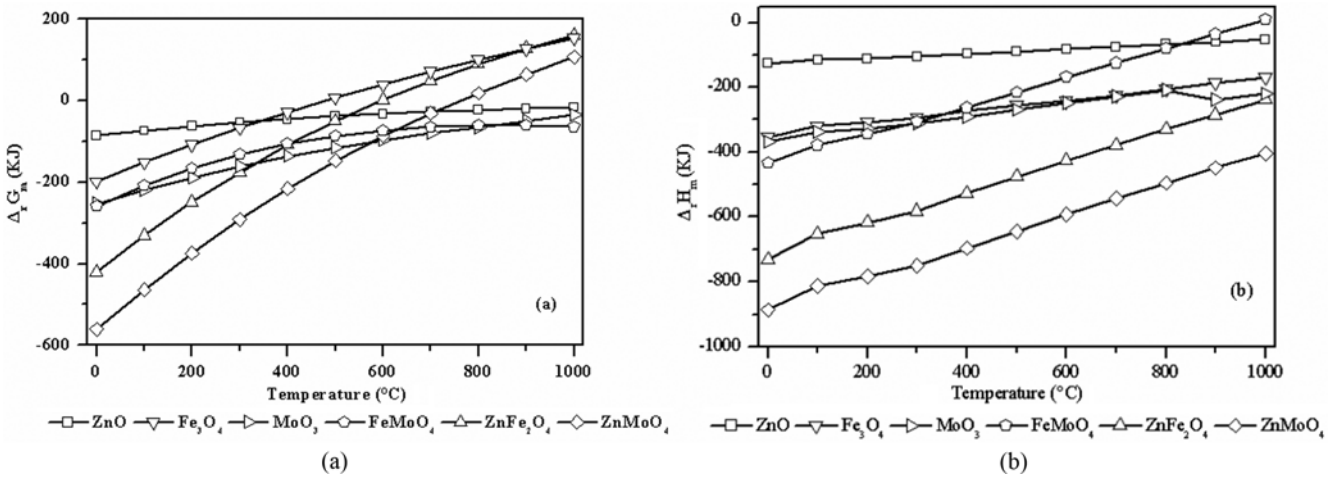

Fig. 11. Thermodynamic properties of different phases in sorbents as a function of temperature: (a) Δ_rG_m vs. temperature; (b) Δ_rH_m vs. temperature.

considered to choose the optimal operating conditions. At any given temperature below 600 °C, the Gibbs free energy ($\Delta_r G_m$) of F10Z6M5 sorbent showed the lowest value and the sulfidation reaction was spontaneous. At higher temperatures, the reaction rate of sulfidation reaction was higher. Consistent with experimental results, thermodynamic calculations also indicate that 400 °C is the optimal desulfurization temperature.

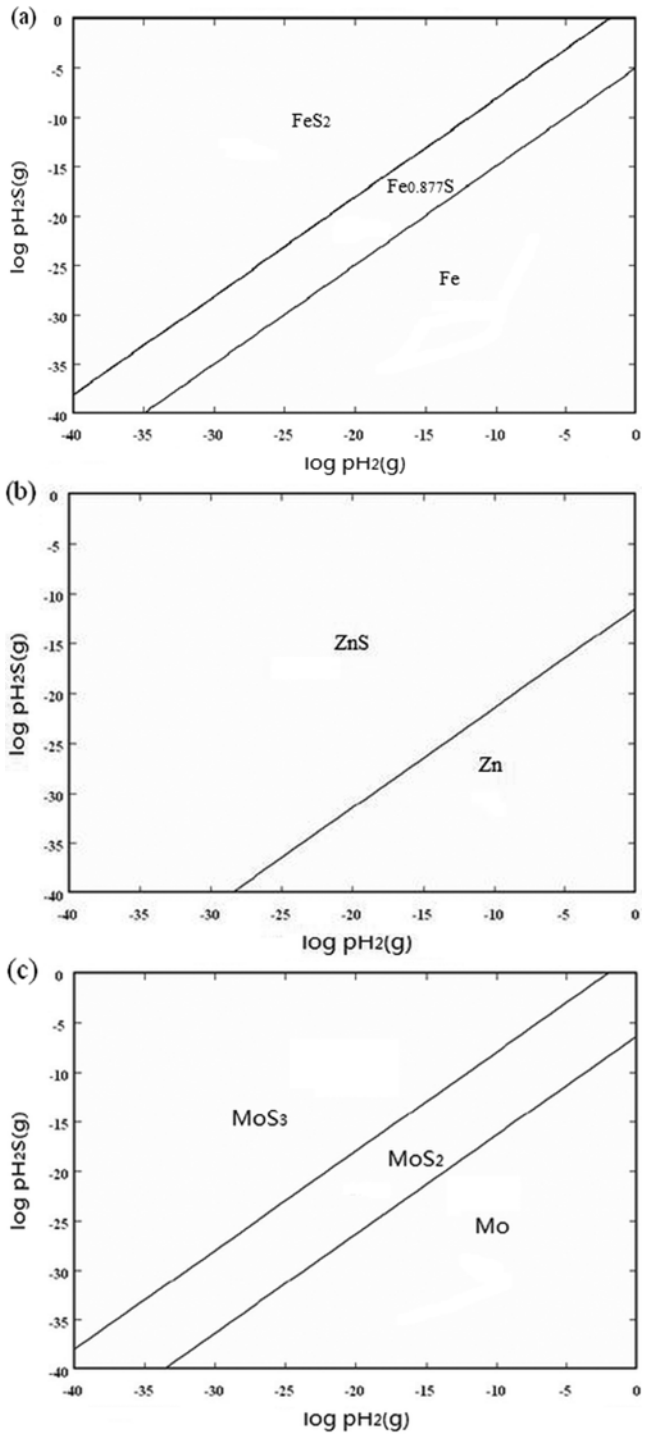

Fig. 12. Thermodynamic prediction of stable phases as a function of partial pressure of H_2S and H_2: (a) iron; (b) zinc; and (c) molybdenum.

Thermodynamic phase diagrams for the sorbent at 400 °C are shown in Fig. 12. It can be seen that FeS_2 and $Fe_{1-x}S$ are preferred over Fe as the thermodynamically stable phase at higher H_2S concentration and lower H_2 partial pressures at 400 °C (Fig. 12(a)). Higher concentration of H_2S and lower concentration of H_2 also favored Fe_3O_4 reaction with H_2S to form FeS_2 and $Fe_{1-x}S$ (x=0.123). Fig. 12(b) shows that ZnS is the thermodynamically stable phase at higher H_2S concentration and lower H_2 partial pressures at this temperature. Zn phase can be formed during desulfurization at higher H_2 partial pressure. Compared to Mo-H_2S-H_2 system, MoS_3 and MoS_2 are the main products when active component reacts with H_2S at lower H_2 partial pressures (Fig. 12(c)). These results were consistent with the XRD analysis. From thermodynamic point of view, H_2S removal at medium temperatures and low H_2 partial pressure is favorable.

CONCLUSION

The addition of Mo significantly improved the desulfurization performance (breakthrough time, sulfur capacity and desulfurization efficiency) of char-supported Fe-Zn sorbents. Desulfurization reactions were exothermic and thermodynamically favorable in the temperature range of 200-400 °C, while higher concentration of H_2S and lower concentration of H_2 favored the reaction of metal oxides with H_2S to form metal sulfides. The BET analysis results showed microporous and mesoporous structures in sorbents with a narrow pore-size distribution of 2-4 nm. Char-supported F10Z6M5 sorbent showed the optimal sulfidation properties at 400 °C.

ACKNOWLEDGEMENTS

The authors acknowledge the financial support from the Natural Science Foundation of China (21176109 and 21476100), the Doctoral Education Programs Foundation of Ministry of Education of China (20112120110002) and Liaoning Outstanding Professorship Funding Program (2012) of Liaoning Province.

REFERENCES

1. J. Leppälahti and T. Koljonen, *Fuel Process. Technol.*, **43**, 1 (1995).
2. A. Vander Drift, J. van Doorn and J. Vermeulen, *Biomass Bioenergy*, **20**, 45 (2001).
3. S. Cheah, D. L. Carpenter and K. A. Magrini-Bair, *Energy Fuels*, **23**, 5291 (2009).
4. S. H. Kang, S. J. Lee, W. H. Jung, S. W. Chung, Y. S. Yun, S. H. Jo, Y. C. Park and J. I. Baek, *Korean J. Chem. Eng.*, **30**, 67 (2013).
5. X. Meng, W. de Jong, R. Pal and A. H. M. Verkooijen, *Fuel Process. Technol.*, **91**, 964 (2010).
6. I. I. Novochinskii, C. Song, X. Ma, X. Liu, L. Shore, J. Lampert and R. J. Farrauto, *Energy Fuels*, **18**, 584 (2004).
7. F. Yin, J. Yu, J. Dou, S. Gupta, B. Moghtaderi and J. Lucas, *Energy Fuels*, **28**, 2481 (2014).
8. X. Zheng, W. Bao, Q. Jin, L. Chang and K. Xie, *Energy Fuels*, **25**, 2997 (2011).
9. H. F. Garces, A. E. Espinal and S. L. Suib, *J. Phys. Chem. C*, **116**,

8465 (2012).
10. W. Xie, L. Chang, D. Wang, K. Xie, T. Wall and J. Yu, *Fuel*, **89**, 868 (2010).
11. M. A. Ahmed, L. Alonso, J. M. Palacios, C. Cilleruelo and J. C. Abanades, *Solid State Ionics*, **138**, 51 (2000).
12. G. Q. Liu, Z. H. Huang and F. Y. Kang, *J. Hazard. Mater.*, **215-216**, 166 (2012).
13. P. Dhage, A. Samokhvalov, D. Repala, E. C. Duin, M. Bowman and B. J. Tatarchuk, *Ind. Eng. Chem. Res.*, **49**, 8388 (2010).
14. Y. C. Park, S. H. Jo, H. J. Ryu, J. H. Moon, C. K. Yi, Y. Yoon and J. I. Baek, *Korean J. Chem. Eng.*, **29**, 1812 (2012).
15. Z. Ozaydin, S. Yasyerli and G. Dogu, *Ind. Eng. Chem. Res.*, **47**, 1035 (2008).
16. R. B. Slimane and J. Abbasian, *Ind. Eng. Chem. Res.*, **39**, 1338 (2000).
17. D. Wang, J. Yu, L. Chang and D. Wang, *Chem. Eng. J.*, **166**, 362 (2011).
18. F. Yin, J. Yu, S. Gupta, S. Wang, D. Wang and J. Dou, *Fuel Process. Technol.*, **117**, 17 (2014).
19. H. Zhao, D. Zhang, F. Wang, T. Wu and J. Gao, *Process Safety Environ. Protection*, **87**, 274 (2009).
20. W. Bao, Z. Y. Zhang, X. R. Ren, F. Li and L. P. Chang, *Energy Fuels*, **23**, 3600 (2009).
21. Z. Y. Wan, B. S. Liu, F. M. Zhang and X. H. Zhao, *Chem. Eng. J.*, **171**, 594 (2011).
22. M. Casu, M. F. Casula, A. Corrias and G. Paschina, *J. Non-Cryst. Solids*, **315**, 97 (2003).
23. E. Sasaoka, K. Taniguchi, S. Hirano, M. A. Uddin, S. Kasaoka and Y. Sakata, *Ind. Eng. Chem. Res.*, **34**, 1102 (1995).
24. B. E. Yoldas, *J. Non-Cryst. Solids*, **63**, 145 (1984).
25. A. Tahmasebi, J. Yu and S. Bhattacharya, *Energy Fuels*, **27**, 154 (2012).
26. W. Chen, F. Li, Y. Chen, K. Yuan and L. Chen, *Appl. Surf. Sci.*, **257**, 8788 (2011).
27. J. Lian, X. Duan, J. Ma, P. Peng, T. Kim and W. Zheng, *ACS Nano*, **3**, 3749 (2009).
28. X. Wang, T. Sun, J. Yang, L. Zhao and J. Jia, *Chem. Eng. J.*, **142**, 48 (2008).
29. Z. Hu, A. Luo, N. Mao, Y. Huang, L. Y. Wei and H. X. Shen, *Acta. Phys. Sin-CH. ED.*, **42**, 1712 (1993).
30. Y. Qin, L. Wu, Y. Kang, Y. Tang, Z. Li, Y. Zheng, R. Chen and Y. Ya, *Spectrosc. Spect. Anal.*, **20**, 663 (2000).
31. J. Yu, F. Yin, S. Wang, L. Chang and G. Sushil, *Fuel*, **108**, 91 (2013).
32. Z. Yan, L. Liu, Y. Zhang, J. Liang, J. Wang, Z. Zhang and X. Wang, *Energy Fuels*, **27**, 3080 (2013).